CONDENSED MATTER PHYSICS

Mechanically reconfigurable van der Waals devices via low-friction gold sliding

Andrew Z. Barabas[1]†, Ian Sequeira[1]†, Yuhui Yang[1], Aaron H. Barajas-Aguilar[1], Takashi Taniguchi[2], Kenji Watanabe[2], Javier D. Sanchez-Yamagishi[1]*

Interfaces of van der Waals (vdW) materials, such as graphite and hexagonal boron nitride (hBN), exhibit low-friction sliding due to their atomically flat surfaces and weak vdW bonding. We demonstrate that microfabricated gold also slides with low friction on hBN. This enables the arbitrary post-fabrication repositioning of device features both at ambient conditions and in situ to a measurement cryostat. We demonstrate mechanically reconfigurable vdW devices where device geometry and position are continuously tunable parameters. By fabricating slidable top gates on a graphene-hBN device, we produce a mechanically tunable quantum point contact where electron confinement and edge-state coupling can be continuously modified. Moreover, we combine in situ sliding with simultaneous electronic measurements to create new types of scanning probe experiments, where gate electrodes and even entire vdW heterostructure devices can be spatially scanned by sliding across a target.

INTRODUCTION

Nanoscale electronic devices are typically static, with the material structure and device geometry set during the fabrication process. Exploring the full parameter space requires fabricating multiple devices with varying geometries and material structures. Ideally, a device's material structure and geometry would be reconfigurable in situ, allowing for post-fabrication modification while simultaneously measuring its properties. Microelectromechanical systems enable a limited range of mechanical reconfigurability at the cost of complex suspended device structures (*1*). For conventional non-suspended devices, mechanical modification of the device structure is typically not possible because of high friction forces at all interfaces.

An exception to this is van der Waals (vdW) layered materials, which exhibit low interfacial friction due to weak vdW bonds, atomically flat layers, and lattice incommensurability (*2*–*8*). Recently, this property has been exploited to perform twist angle–dependent studies of graphite and graphene-based heterostructures by sliding vdW flakes with an atomic force microscope (AFM) (*9*–*12*). This approach is powerful, but currently limited by difficulties in fabricating complex vdW heterostructures, as well as the need to perform experiments in ambient conditions.

Here, we show that microfabricated gold exhibits low-friction sliding on hexagonal boron nitride (hBN), a vdW material, at both ambient conditions and cryogenic temperatures (7.6 K). The low-friction gold-hBN interface enables us to produce a wide range of slidable structures to form mechanically reconfigurable vdW devices, including a tunable graphene quantum point contact (QPC) and sliding-based scanning probe devices. These devices can be modified ex situ in an AFM or in situ in a measurement cryostat.

[1]Department of Physics and Astronomy, University of California, Irvine, Irvine, CA, USA. [2]Research Center for Functional Materials, National Institute for Materials Science, 1-1 Namiki, Tsukuba, Japan.
†These authors contributed equally to this work.
*Corresponding author. Email: javier.sanchezyamagishi@uci.edu

RESULTS

Low-friction gold on hBN

We create reconfigurable structures by depositing gold microstructures directly onto hBN flakes using electron beam lithography (EBL) and electron beam evaporation (see the "Friction measurements" section in Materials and Methods for fabrication details). By pushing laterally with an AFM tip, we can slide microscale, polycrystalline gold features as large as 35 μm^2 across the hBN surface. The low-friction sliding enables arbitrary repositioning of deposited features (Fig. 1, A and B). We observe that small features can even be moved by scanning an AFM tip in tapping mode. The motions are nondestructive, with no change to either the gold or hBN observable in AFM except for the cleaning of contaminants on the hBN surface, which are swept away by the sliding gold (Fig. 1C).

To characterize the friction, we slide gold squares of different sizes on hBN using an AFM tip and determine the interfacial friction from AFM deflection measurements, similar to previous vdW tribological studies (*4*–*6*, *8*, *13*, *14*). Figure 1D illustrates the friction measurement scheme. First, the tip is moved laterally at a fixed z-piezo extension elevated above the hBN surface (left). Once the tip makes contact with the edge of the stationary gold square, it deflects laterally, resulting in a voltage signal on the AFM photodiode (middle). The lateral deflection increases until the static friction of the gold-hBN interface is overcome, after which it drops to a constant value corresponding to the kinetic friction as the gold slides on the hBN (right). These regions are highlighted in an example deflection trace in Fig. 1E, where the peak (static) voltage and constant (kinetic) voltage are indicated.

To determine the scaling of friction with interface size, we repeat these measurements multiple times each for 0.5- to 3-μm-wide gold squares and observe a linear scaling of deflection voltages versus area, with slopes of 82 ± 6 mV/μm^2 (static) and 24.4 ± 0.6 mV/μm^2 (kinetic). Assuming that force is directly proportional to deflection voltage, our data show that interface friction scales linearly with area, which is expected for polycrystalline interfaces (*14*). By contrast, atomically flat and lattice incommensurate interfaces, including single-crystal gold nanoparticles on graphite, can exhibit

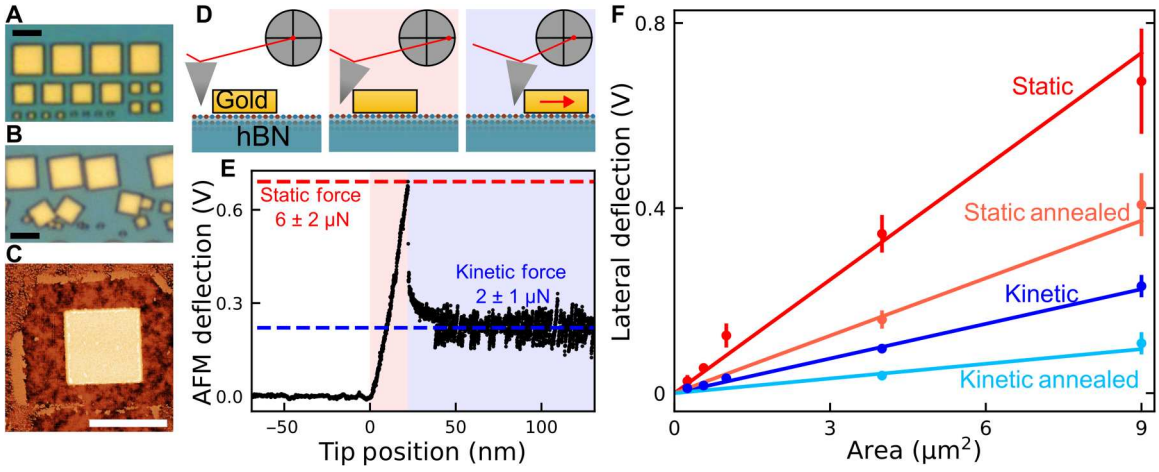

Fig. 1. AFM friction measurements for gold squares sliding on hBN. Scale bars, 3 μm. (**A** and **B**) Optical images of ~170-nm-tall gold squares on hBN before and after manipulation with an AFM tip. (**C**) AFM height image of a 3-μm-wide gold square on atomically flat hBN surface with contaminants swept aside by sliding. The root mean square roughness of the swept hBN is 1 Å, and the height of the surface contaminants is roughly 8 nm. A nonlinear color scale is used to highlight features across a wide range of heights. (**D**) Schematic illustrating AFM lateral friction measurement: before contact (left), during static friction (middle), and during kinetic friction (right). (**E**) AFM friction linetrace for a 3-μm-wide square with the tip moving at 1 nm/s. The peak voltage corresponds to the Au-hBN static friction, and the subsequent constant voltage corresponds to the kinetic friction. (**F**) Lateral deflection voltage versus interface area between gold and hBN for 0.5-, 0.75-, 1-, 2-, and 3-μm-wide squares before and after annealing at 350°C for 30 min. Each data point is the average of multiple measurements for each size. Error bars show SD. Lines are linear fits through zero, fitting only the 4 and 9 μm^2 data points; this excludes smaller deflection data points that have variable AFM sensitivity (see the "Friction measurements" section in Materials and Methods for more details).

sublinear scaling versus area (*3*, *4*, *8*, *14*). This suggests that increasing the grain size of our gold will decrease interface friction. To test this, we vacuum-annealed our samples at 350°C for 30 min and observed that the deflection voltages decrease by 50%. The annealing process also caused the average gold grain size to increase from ~20 to ~80 nm, suggesting a connection, although the removal of contaminants from the Au-hBN interface by heat annealing likely plays a role as well.

We convert the AFM deflection voltage to a lateral force using a linear model that requires both the AFM tip's lateral spring constant and the AFM's lateral sensitivity. The spring constant is the ratio of lateral force applied to the tip and lateral displacement, which we determine by simulating our tip in COMSOL Multiphysics. In addition, the sensitivity is the ratio of lateral tip displacement and lateral deflection voltage measured on the AFM photodiode. To measure the lateral sensitivity, we use the slope of the static region of our deflection linetraces (see the "Friction measurements" section in Materials and Methods for more details).

Converting the deflection voltages yields forces of 6 μN (static) and 2 μN (kinetic) for a 9-μm^2 gold square on hBN. Applying the conversion to the linear fits results in a friction force per unit area. For the unannealed Au-hBN interface, the friction values are 800 $nN/\mu m^2$ (static) and 230 $nN/\mu m^2$ (kinetic), and after annealing, they decrease to 400 and 100 $nN/\mu m^2$, respectively. These force values have uncertainties of 30%, dominated by uncertainty in the sensitivity, and should be considered upper bounds due to the calibration method and limitations of the linear model (see the "Friction measurements" section in Materials and Methods). These interfacial friction values are comparable to prior tribology studies of gold on graphite, which measured 50 to 430 $nN/\mu m^2$ (kinetic) for ~60- to ~100-nm-wide, single-crystal, gold nanoparticles (*13*). For additional comparison, the previously reported kinetic friction of unaligned graphite on hBN is smaller, at 15 $nN/\mu m^2$ (*5*). We have also made friction measurements of gold with a 3-nm Cr sticking layer on hBN, and initial tests show that it exhibits roughly an order of magnitude higher friction than annealed gold on hBN without a sticking layer (see fig. S3).

Mechanically tunable QPC

The low friction between Au-hBN enables studies of vdW quantum devices in which reconfigurable gold gates are used to mechanically modify electron confinement. Gate-defined QPC and quantum dots are of particular interest as they are integral for making graphene-based qubits (*15*–*17*) and for studying non-Abelian quasiparticles (*18*, *19*).

We apply this unique confinement control capability to make a reconfigurable QPC defined by movable gold-only top gates on an hBN-encapsulated graphene device (Fig. 2A). The top gates confine electrons by depleting the graphene into a bandgap, thereby forming a narrow QPC constriction between two conducting regions. Although graphene lacks an intrinsic bandgap, one forms in a perpendicular magnetic field at zero density due to exchange interactions (*20*). Therefore, in the quantum hall regime, we can study the edge mode transmission through the constriction at different Landau level filling factors and QPC separations by holding the dual-gated region at the charge neutrality point while sweeping the back-gate voltage (*21*, *22*).

To adjust the QPC separation, the top gates are physically moved with an AFM tip at ambient conditions, modifying the QPC confinement mechanically (Fig. 2A). We then cool the sample to 1.5 K, apply a 9-T out-of-plane magnetic field, and measure the resistance versus top-gate and back-gate voltages. From these measurements, we determine the QPC conductance, referred to as G_{QPC}, by taking the inverse of the measured resistance after subtracting a contact

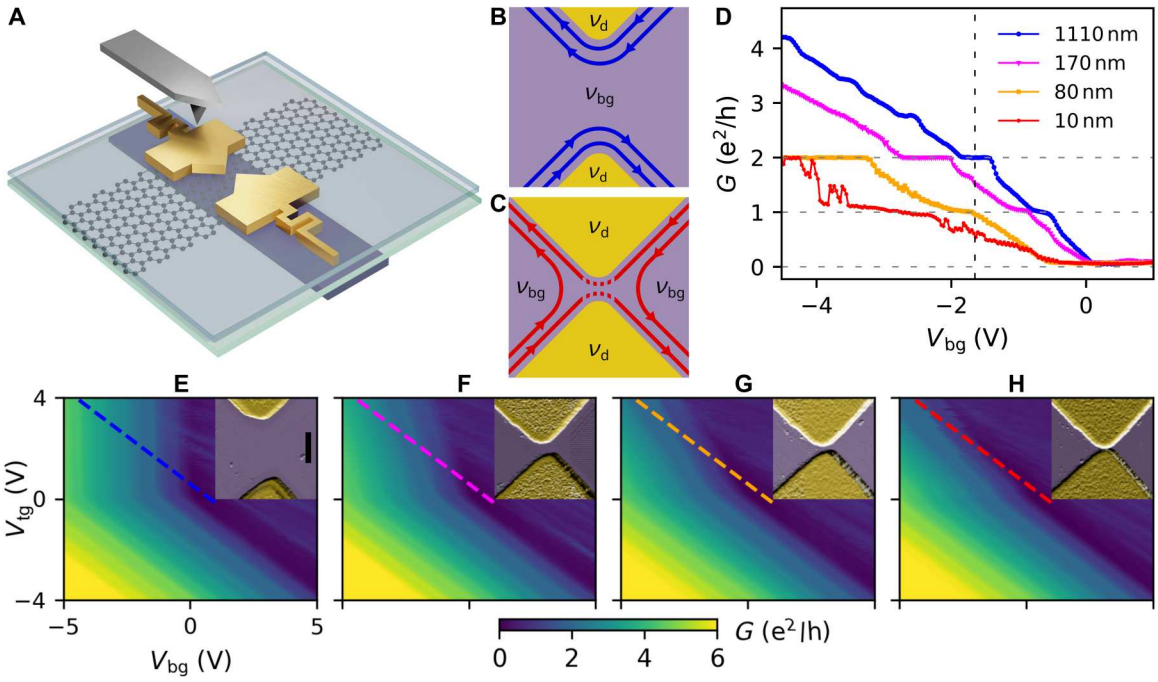

Fig. 2. Measurement of a mechanically reconfigurable QPC device. (**A**) Schematic of an hBN-encapsulated graphene device with a local graphite back gate and flexible serpentine leads connected to the movable QPC top gates (metal contacts to the graphene and graphite not shown). (**B** and **C**) QPC edge mode schematic for $\nu_d = 0$ and $\nu_{bg} = -2$. (B) For a large QPC separation, all edge modes are completely transmitted, as in the 1110-nm separation. (C) Reduced QPC separation such that the innermost edge mode is completely backscattered, while the outer edge mode is partially backscattered (indicated by the dotted lines), as in the 10-nm separation. (**D**) Linecuts of full 2D conductance color plots taken at 9 T and 1.5 K along $\nu_d = 0$ for each of the four separations. The vertical dashed line at $V_{bg} = -1.65$ V indicates the $\nu_{bg} = -2$ filling. (**E** to **H**) Conductance color plots versus graphite back-gate and QPC top-gate voltages at separations of 1110, 170, 80, and 10 nm, respectively. Dashed lines correspond to $\nu_d = 0$ linecuts presented in (D). Insets are false color AFM amplitude images of QPC gates. Scale bar in (E) is 500 nm and applies to all AFM images.

resistance (see the "QPC device" section in Materials and Methods and the Supplementary Materials for more details).

Adjusting the QPC separation modulates the tunneling coupling between counterpropagating edge modes, thereby tuning their transmission through the QPC constriction. This is illustrated in Fig. 2 (B and C), which shows different gate separations of the QPC but at identical gate voltage conditions. The Landau level filling factors shown are $\nu_{bg} = -2$ for the back gate and $\nu_d = 0$ for the dual-gated regions. When the QPC separation is large, edge modes transmit across the device unimpeded, resulting in a G_{QPC} of 2 e^2/h (Fig. 2B). In contrast, at the same filling factors, a smaller QPC separation causes the counter-propagating edge modes to tunnel couple and backscatter, decreasing $G_{QPC} \leq 2$ e^2/h (Fig. 2C).

We measure the QPC conductance with $\nu_d = 0$ for four separations: 1110, 170, 80, and 10 nm (Fig. 2D). It is apparent that physically narrowing the QPC generally decreases G_{QPC} at a given back-gate voltage. At filling factor $\nu_{bg} = -2$ (vertical dashed line at $V_{bg} = -1.65$ V), a 2 e^2/h plateau is observed for the 1110-nm separation, corresponding to the edge modes in the back-gated region transmitting across the device unimpeded, equivalent to Fig. 2B. At the same filling factor, narrowing the QPC separation to 170 nm decreases G_{QPC} to between 1 and 2 e^2/h, indicating partial reflection of one edge mode. Further narrowing to 80 nm results in a 1 e^2/h plateau. This surviving quantized plateau is explained by the spatial separation of the edge modes. The innermost counterpropagating modes are close enough to completely backscatter via tunneling, while the outer modes are still too far apart to couple and instead transmit through the QPC fully. Narrowing the QPC separation further to 10 nm results in partial reflection of the remaining edge mode such that $G_{QPC} < 1$ e^2/h (as illustrated in Fig. 2C). Similarly, for $\nu_{bg} = -1$ ($V_{bg} = -0.65$ V), a 1 e^2/h plateau is observed in the 1110-nm separation, which we reduce to 0.14 e^2/h by narrowing the QPC separation, demonstrating our ability to mechanically pinch-off the conductance. In the full device conductance map (Fig. 2, E to H), the gate voltage region where pinch off is attained (right of diagonal line) grows in size as the gate separation is reduced.

The mechanical gate tuning we demonstrate offers an unprecedented level of control, as confinement geometry and physical position of the QPC can be modified independent of gate voltages. Such an approach will be highly useful for tuning the properties of gate-defined quantum dots and QPCs in vdW heterostructures.

In situ heterostructure and cryogenic manipulation

An exciting aspect of the low friction between gold and hBN is the potential for true in situ manipulation of a device's atomic structure. Here, in situ means simultaneous manipulation and measurement under the extreme conditions often required for quantum experiments, such as cryogenic temperatures, high magnetic fields, and high vacuum. Of these conditions, cryogenic manipulation presents the biggest challenge because friction typically increases

significantly at low temperatures due to reduced thermal vibrations and the freezing of gas within the cryogenic vacuum space (*23*).

To advance vdW manipulation beyond pushing individual flakes at ambient conditions, we aim to achieve deterministic lateral motion of flakes and even whole heterostructures by creating a rigid mechanical connection to them. The conventional method for vdW flake manipulation, as demonstrated in Figs. 1 and 2 and prior works (*9*–*12*), uses a sharp AFM tip to push a flake from the side and then reimages the flake position using the same tip. This, however, does not result in deterministic, one-to-one motion of the flake and makes certain manipulation applications, such as scanning, infeasible. Likewise, this manipulation technique is not well suited to overcome the high friction forces at cryogenic temperatures and for large interface areas due to the small contact area between the sharp tip and the flake. We encounter the limits of this style of motion with very large gold contacts in our QPC devices (area > 35 μm^2), which are cut by the AFM tip as it pushes laterally. To address these issues, we have created metal handles that interface the AFM tip to a vdW heterostructure.

The handle grips the vdW flakes/heterostructures by overlapping the flake edges so that it conforms to the flake and distributes force along the flake's edges. We press-fit a flattened AFM tip into a donut-shaped hole in the handle, which deforms the metal to match the tip shape and provides increased grip. This strong connection enables deterministic sliding of gold on hBN at cryogenic temperatures (T = 7.6 K; see Fig. 3A and movie S1).

Despite the increased friction at cryogenic temperatures, as evidenced by visible tip flex in movie S1, we observe that the hBN surface is left pristine and undamaged after more than 100 motions at a speed of 30 μm/s (Fig. 3B). See the "In situ sliding" section in Materials and Methods for details about the manipulation technique and setup. Cold sliding can enable a variety of experiments including reconfigurable vdW heterostructures at cryogenic temperatures, which would allow for rapid, continuous measurements with respect to physically reconfigurable parameters.

While mechanical linkage and motion is useful in its own right, electrical contact to moveable structures is also critical to perform many experiments. To this end, we fabricate flexible serpentine-shaped electrodes connected to our donut handles, which are anchored at one end of the hBN flake on SiO_2, shown in Fig. 3C. We are able to oscillate these electrodes at 10 Hz with an amplitude of 2 μm by actuating with an AFM tip and the same donut interface described above (video available online). We find that these accordion geometries with a wire cross section of 1 μm thick and 1 μm wide are able to stretch over 10 μm before breaking. Note that, except for extreme displacements, the friction force is high enough to prevent the electrodes from springing back when the AFM tip is disengaged.

By combining mechanical motion and flexible electrodes, we create a sliding scanning top gate, shown in Fig. 3 (D to F). At room temperature, we raster a gold top gate by sliding it over an encapsulated graphene-hBN device, modulating the device resistance

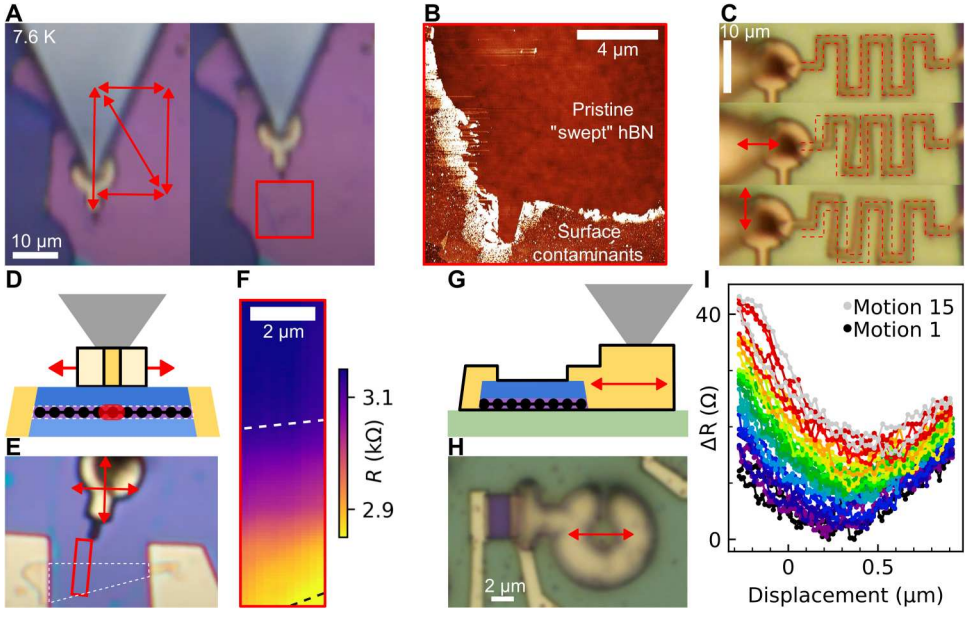

Fig. 3. In situ mechanically reconfigurable devices. (**A**) Optical images showing gold sliding on hBN (pink) at 7.6 K, actuated by an AFM tip (gray). Arrows denote the range and direction of motions. Dark purple on the left is the SiO_2 substrate. See movie S1 for a video recording of the motions. (**B**) AFM image of hBN surface after cryogenic scanning motions from (A) showing that the hBN surface is left undamaged with only swept-up surface contaminants. AFM area is the solid red boxed area in (A). (**C**) Optical images of gold serpentine electrodes on hBN (pale yellow/green) showing ~2-μm longitudinal and transverse motions. Red dotted lines outline the initial position. Video recordings of oscillating motion shown in movies S2 and S3. (**D**) Side profile schematic of a sliding top-gate hBN-encapsulated graphene device, actuated with an AFM tip. Top-gate slides over stationary graphene to change local gating and device resistance. (**E**) Top-down optical image of the same device. The graphene is outlined with a dotted white line, and the light purple background is hBN. Red rectangle is 2.4 × 9.5 μm. (**F**) Graphene resistance versus top-gate position. Scanning range shown as the red rectangle in the optical image. Dashed lines indicate graphene edges. (**G**) Side profile schematic of a slidable graphene-hBN device on a stationary hBN substrate, actuated with an AFM tip. The slidable features in the schematic are outlined in black. (**H**) Top-down optical image of the same device. The pale green background is hBN. (**I**) Two-probe resistance of the slidable graphene device versus sliding position (see movie S4 for the video recording). 0 μm corresponds to the initial, transferred position. The increase in resistance over subsequent motions is likely due to photodoping from the light source used for imaging.

by changing the overlap between the graphene and top gate. The resistance versus gate position is plotted in Fig. 3F, which can be interpreted as a coarse image of our graphene device convolved with the geometry of the sliding gate. This constitutes a new mechanism for scanning probe microscopy (*24*), where a scanned gate is in direct atomic contact with the sample, obviating the need for the feedback control of the probe-sample distance that is typical with scanning probes.

Taking advantage of the low friction of both graphene-hBN and Au-hBN interfaces, we apply our technique to make a slidable, contacted vdW heterostructure, shown optically and schematically in Fig. 3 (G and H). Here, an entire graphene device is translated over an hBN substrate, actuated via a metal handle. The graphene, edge-contact electrodes, and top hBN all slide as a single unit and allow for continuous measurement of the graphene as it is moved. Figure 3I shows the change in graphene resistance as it is translated back and forth. As the graphene slides 1.2 μm, we observe a reproducible modulation of the device resistance corresponding to a maximum change of 10 to 15 ohms. Naively, one would not expect any change in the graphene resistance due to translating the device. One explanation for this effect is that the graphene is gated by charge inhomogeneity in the hBN (*25*), modulating its resistance and causing it to act as a local charge sensor. Another effect that can arise in this device geometry is strain in the graphene or at the graphene-gold interface that develops in response to friction forces during the motion. These effects will be isolated and explored in future studies.

DISCUSSION

The ability to move both metal and vdW layers within a device offers an unprecedented level of control and flexibility in both device function and experiment design. The mechanically reconfigurable devices we demonstrate enable experimental studies where structure and geometry are continuously tunable parameters. This allows for dense sampling of the device and heterostructure parameter space while keeping local disorder constant, something that is impossible to achieve with the conventional approach of fabricating multiple devices. Reconfiguration by sliding makes possible the modification of quantum confinement via moveable gate electrodes, as well as the continuous tuning of lattice interfaces in vdW moire heterostructures. Our demonstration of deterministic in situ sliding also introduces the possibility of dynamic structural studies, where time-varying modulations of the device geometry, strain, and interfacial moires induce electronic effects such as topological charge pumping (*26*–*28*). Last, the proof-of-principle sliding scanning probe experiments show a new approach to spatial mapping of local material properties at the extreme limit of proximity, i.e., direct atomic contact, as well as with the full flexibility of planar nanofabrication.

MATERIALS AND METHODS

General fabrication techniques

The following techniques are universal to our device fabrication except when specified otherwise.

Lithography

All lithography performed is EBL using a poly(methyl methacrylate) (PMMA) resist. We use PMMA 950 A5 spun at 2000 rpm for 2 min, resulting in a ~500-nm-thick layer for depositions less than 300 nm in thickness and for etch masks. EBL patterns are written at 1.6 or 3.2 nA with 30-kV excitation. The PMMA is developed for 3 min in a cold mixture of 3:1 isopropyl alcohol (IPA)/water.

One-dimensional edge contacts

One-dimensional (1D) edge contacts for our graphene encapsulated in hBN devices are written with EBL and developed before reactive ion etching with 10 standard cubic centimeters per minute (SCCM) of SF_6, 2 SCCM of O_2, 30 W of radio frequency power, at 100 mtorr for 30 s (*29*). Then, 3 nm of Cr and ~100 nm of Au are deposited at 1 Å/s in an electron beam metal vapor deposition system. Liftoff is performed by soaking the sample in acetone for 1 to 2 hours and agitating with a pipette.

Exfoliation and dry transfers

We exfoliate hBN and graphene from bulk crystals. Stacks are assembled using stamps consisting of polycarbonate (PC) film on a polydimethylsiloxane (PDMS) square on a glass slide (*30*). We have used hBN ranging from ~15 to ~230 nm thick as a substrate for sliding gold structures.

Friction measurements

Fabrication for gold-hBN friction measurements

Gold-only squares for friction measurements are fabricated by spinning PMMA on a silicon chip of exfoliated hBN, writing squares using EBL, depositing 170 nm of gold, and lifting off in acetone.

AFM lateral friction measurements

To measure lateral friction, we use the lithography mode of a Park Systems NX10 AFM and a Budget Sensors Tap300Al-G tip to manipulate gold on hBN in ambient conditions. First, the top surface of the gold squares is measured using lithography set point mode with 100 nN of downward force and a dwell time of 8 s. The tip is then moved next to the gold square, lowered 100 nm below the top surface of the gold, and moved laterally, transverse to the AFM cantilever, and into the gold square at 10 nm/s. The lateral deflection voltage is recorded throughout the motion. Measurements were also made at 1 and 100 nm/s, and no dependence on speed was observed in this range. Care is taken for the motion to be through the center of mass of the gold to avoid rotation, and motions with rotation are excluded from our analysis. The squares are also oriented, so their edge is perpendicular to the direction of motion. Note that no permanent deformation of the gold is observed in AFM images taken after manipulations.

The regions before contact, during static friction, and during kinetic friction are identified to extract the average baseline voltage, average kinetic friction, and the peak static friction value, respectively. We include some example linetraces to demonstrate the scales and overall appearance of typical linetraces (fig. S1). Although some traces do not exhibit the ideal lineshape, their kinetic and static friction values do not deviate from other traces. The exact mechanisms that cause nonidealities are not clear. To measure force using the AFM, we assume a linear model where deflection voltage is related to the force on the cantilever as $F_{tip} = V_{tip}\, k/S$, where V_{tip} is the lateral deflection voltage of the AFM tip, k is the tip spring constant, and S is the AFM sensitivity.

The cantilever is simulated in COMSOL Multiphysics to determine its spring constant, referencing optical and scanning electron microscopy images for its dimensions (*6*). To simulate the spring constant, a lateral force is applied 100 nm above the apex of the

tip and the displacement at this position is determined, resulting in a force per distance displaced of $k = 250 \pm 10$ N/m for our tip. The simulations are parameterized with respect to the cantilever dimensions to estimate an uncertainty for the lateral spring constant. The material used is single-crystal anisotropic silicon with the top of the cantilever as the <100> plane and the cantilever pointing in the <110> direction.

To determine the sensitivity, S, which is the ratio of the lateral voltage deflection to tip displacement, we take the slope of the static region of the deflection linetrace when the tip deflects before the gold starts moving. This assumes that the lateral displacement of the AFM piezo stage is equal to the tip deflection during the static portion of the pushing. However, we expect the tip deflection to be less than the stage displacement due to other effects, such as the elastic deformation of the gold, or due to the tip slipping as it comes into contact with the gold edge. These effects are evidenced by nonlinearity in the slope of the static region and by the variable sensitivities we observe for smaller squares. The net effect is that our approach will overestimate the displacement of the cantilever, which would result in our extracted forces providing an upper bound on the friction force. Because of the variable sensitivity we observe for smaller squares (1 μm^2 and smaller), we only use the 4- and 9-μm^2 linetraces to calculate an average lateral sensitivity of $S = 27 \pm 8$ mV/nm.

Annealing gold on hBN

To test the effect of heat annealing, the gold squares on hBN are vacuum-annealed for 30 min at 350°C in a tube furnace. Measuring their friction again, we see that the tip deflections decreased by ~50%. AFM imaging shows that the grain sizes increased from ~20 to 80 nm in diameter. This qualitative behavior is expected for polycrystalline materials, but it may also be the result of trapped contaminants escaping from the gold-hBN interface.

QPC device

QPC device fabrication

Our reconfigurable QPC device consists of a graphene strip encapsulated in hBN, with a local graphite back gate on a Si/SiO_2 substrate. 1D edge contacts are added to the graphene and graphite back gate. The moveable top gates are 170-nm-thick gold-only deposited with long, flexible electrodes to allow the gates to be moved while maintaining electrical contact. The Au-hBN interface friction is relatively large for the top gates and flexible electrodes due to their large surface area. To avoid cutting the gates while attempting motions, we cross-link 500-nm-tall PMMA rectangles onto the gates (fig. S4A). These tall features provide more surface area for the AFM tip to push into to move the top gates. Although they still deform from manipulations, they serve as a sacrificial handle. We dose the PMMA with 15,000 $\mu C/\mu m^2$ at 30 kV and 3.2 nA to cross-link it. A small, isolated square of gold is also deposited onto the hBN (at the same time as the gold-only top gates) to sweep contaminants from the hBN surface, seen in fig. S4B.

To determine the QPC constriction width, we measure the top-gate separation using AFM. Because of the height of the top gates, the separation at the base of the gate differs from what is observed using a standard AFM tip. To account for this, we measure the sidewall profile using a Nanosensors ATEC-NC cantilever and subtract that from what is measured with our standard tips, referencing features on the top surface of the gate.

The graphite back gate for our device is smaller than the graphene. This is so that the 1D edge contacts to the graphene do not short to the back gate. We refer to regions of the graphene that are not gated by the graphite as the graphene contacts, and they are doped to a higher carrier density by the silicon back gate.

QPC measurement details

The resistance data were taken in a four-probe configuration by measuring the current at the drain electrode via a Femto current preamplifier (1E6 V/A gain) and the longitudinal voltage drop with an SR830 lock-in amplifier using low-frequency lock-in techniques. Before performing the 2D gate sweeps, we hole-dope the graphene contacts by biasing the silicon back gate with −45 V corresponding to a filling factor of ~7 at 9 T (nominal 285 nm SiO_2 thickness). For this reason, when both the dual-gated and back-gated regions are electron doped, the device is unable to effectively transmit quantum hall edge modes across the resulting pn junction, and it appears insulating as evident in the upper right corner of each conductance color plot in Fig. 2 (E to H).

In situ sliding

Metal handle and flexible serpentine electrode fabrication

To fabricate the "thick" metal handles and flexible serpentine electrodes for in situ sliding, much thicker PMMA than normal is used: 950 A11 spun at 4000 rpm for 5 s and then 2750 rpm for 2 min. This produces a film of PMMA that is ~2.25 μm thick. EBL is performed using our standard parameters described in the "General fabrication techniques" section. The metal deposition consists of 80 nm Au, 10 nm Cr, 1 μm Cu, 10 nm Cr, and 50 nm Au, all at 1 Å/s, except for the copper, which is deposited at 3 Å/s. The bottom layer of gold is for low friction with the hBN substrate, the top gold protects against oxidation, and the chromium acts as a sticking layer between the gold and copper.

Flexible serpentine electrode widths (1 μm and 500 nm) were tested, and we find that 500-nm-wide electrodes are more flexible but also more fragile. Both work well for manipulation, but we prefer the 500 nm because of the decreased interface area and, hence, reduced friction. We have also fabricated 1-μm and 500-nm-wide "thin" serpentine electrodes, which are 150-nm-tall gold-only instead of the thick multilayer metal combination, and find that the 500-nm-wide electrodes are quite fragile in this case and can break more easily.

Typical metal handle donut dimensions we use have a nominal inner diameter of 3 μm and an outer diameter of 9 μm. The C shape is to help with liftoff as well as to add compliance in being stretched open upon press-fitting with the AFM tip.

In situ manipulation technique

Before performing in situ manipulations using our metal handles, we first flatten a 100 N/m, 1200 MHz MicroMasch 4XC AFM tip to increase the tip-handle contact area. This is carried out by oscillating the tip back and forth and side to side while in contact with SiO_2 of our sample until it is >3 μm wide, slightly larger than the inner diameter of the donut. We choose this tip for its high force constant and the protruding "tip view" style, which makes it easier to align with the donuts.

In general, our technique for performing in situ manipulations involves the sample with a metal handle donut mounted on an XYZ piezo scanner that engages into a stationary flattened AFM tip. This process is carried out by first aligning the donut with the tip and raising the piezo stage. The stage is raised until the donut contacts

the tip, as determined by optically observing a change in the light reflected off the cantilever (seen through a 20× objective). After the initial contact, we press-fit the tip into the donut by raising the stage further. At room temperature, we engage the donut into the tip by ~1.5 to 2.5 μm to achieve a rigid connection with the structures shown in Fig. 3C. In higher-friction situations, such as for larger objects or at cryogenic temperatures, engaging more than ~2.5 μm, corresponding to a larger downward force of the tip on the donut, is necessary to reduce the slippage between the tip and donut and to achieve deterministic, one-to-one sliding motions. For the sliding done at 7.6 K, we engaged ~5 μm as opposed to ~2.5 μm at room temperature to get a similar one-to-one deterministic motion. When finished, the tip can be removed by lifting it from the donut, which results in a slight lateral motion.

Room temperature manipulation setup

Room temperature in situ sliding experiments, including the scanning top gate and the sliding graphene "hockey puck" heterostructure, were performed at ambient conditions. The setup consists of an AFM tip glued to a glass slide, mounted on a coarse manual XYZ stage, and the sample/chip carrier mounted on a Thorlabs 3-axis NanoMax open loop piezo stage. A Mitutoyo VMU microscope with 20× and 2× objectives is used for optical imaging. In both the room temperature and cryogenic manipulation setups, nanomanipulation is performed using the piezo positioners, which are brought into range by coarse screw-based positioners.

Cryogenic manipulation setup

Cryogenic manipulations are performed in a continuous flow Janis ST-500 optical cryostat using the same microscope as for the room temperature manipulation setup. ST-500 is cooled using a Janis helium recirculation setup and achieves a sample temperature of 7.6 K. The sample is mounted on an Attocube ANSxyz100std/LT piezo scanner (with 55 μm of XY range and 25 μm of Z range at ~4 K), and the AFM tip is mounted to a custom flexural positioner for coarse positioning at room temperature (fig. S6). Accounting for thermal contraction, the tip is coarsely positioned at room temperature so that it will be within the piezo scanner range of the sample once at base temperature.

Sliding hockey puck heterostructure

We fabricate our encapsulated slidable graphene hockey puck device by transferring ~200-nm-thick top hBN onto monolayer graphene, writing rectangular PMMA etch masks, and etching with SF_6 and O_2 (same recipe as 1D edge contacts) to leave behind rectangles of hBN on graphene. We then write and deposit 150-nm gold-only "wrap-around contacts," which provide edge contacts to the graphene. The thick top hBN and wrap-around contacts add mechanical support to prevent buckling and provide a rigid grip to hold the hockey puck heterostructures together while it is translated. The hockey pucks are picked up using a PC/PDMS stamp and transferred onto a large bottom hBN substrate before writing and depositing thick flexible electrodes and donuts to electrically contact and manipulate them in situ. Of the five hockey puck devices we attempted to transfer and electrically contact, all but one were successfully contacted (fig. S7F).

Two-probe resistance measurements were performed by current biasing and measuring the voltage drop across the device to determine the resistance. The resistance versus displacement trace was measured by displacing in 10-nm steps and then recording the resistance after a short pause. Here, we refer to the full forward and backward measurement sequence as a single "motion." Each motion takes about 30 s. A video of the motions was recorded, and a light source illuminated the sample during all of the measurements. In addition, all measurements were performed with the silicon back gate grounded.

In Fig. 3D, the zero position corresponds to the initial transferred position of the hockey puck before any motion. After being transferred and contacted, the device was slid to the leftmost position, at about −275 nm, before the subsequent 1.2-μm back-and-forth motions.

Scanning top-gate device

The scanning top-gate device was fabricated by encapsulating graphene in hBN and 1D edge-contacting it. For this device, the thick metal top-gate serpentine electrode structure was initially written and deposited on a separate SiO_2 chip and then picked up and transferred onto the completed graphene device using a PC/PDMS stamp. This electrode was transferred to a position so that one end overlapped with a previously written Cr/Au contact, which provided the electrical connection to the top gate as well as a high friction anchor point (fig. S8).

Two-probe resistance measurements were performed in an identical manner to the sliding hockey puck device described earlier with the addition of two dimensions of motion. The fast scan direction was perpendicular to the graphene channel. The top-gate voltage was held at 0 V for the data presented here.

Supplementary Materials

This PDF file includes:
Supplementary Text
Figs. S1 to S8
Legends for movies S1 to S4

Other Supplementary Material for this manuscript includes the following:
Movies S1 to S4

REFERENCES AND NOTES

1. S. D. Senturia, *Microsystem Design* (Kluwer Academic Publishers, 2002).
2. M. Dienwiebel, G. S. Verhoeven, N. Pradeep, J. W. M. Frenken, J. A. Heimberg, H. W. Zandbergen, Superlubricity of graphite. *Phys. Rev. Lett.* **92**, 126101 (2004).
3. O. Hod, E. Meyer, Q. Zheng, M. Urbakh, Structural superlubricity and ultralow friction across the length scales. *Nature* **563**, 485–492 (2018).
4. E. Koren, E. Lörtscher, C. Rawlings, A. W. Knoll, U. Duerig, Adhesion and friction in mesoscopic graphite contacts. *Science* **348**, 679–683 (2015).
5. Y. Song, D. Mandelli, O. Hod, M. Urbakh, M. Ma, Q. Zheng, Robust microscale superlubricity in graphite/hexagonal boron nitride layered heterojunctions. *Nat. Mater.* **17**, 894–899 (2018).
6. H. Rokni, W. Lu, Direct measurements of interfacial adhesion in 2D materials and van der Waals heterostructures in ambient air. *Nat. Commun.* **11**, 5607 (2020).
7. Z. Liu, J. Yang, F. Grey, J. Z. Liu, Y. Liu, Y. Wang, Y. Yang, Y. Cheng, Q. Zheng, Observation of microscale superlubricity in graphite. *Phys. Rev. Lett.* **108**, 205503 (2012).
8. M. Liao, P. Nicolini, L. Du, J. Yuan, S. Wang, H. Yu, J. Tang, P. Cheng, K. Watanabe, T. Taniguchi, L. Gu, V. E. P. Claerbout, A. Silva, D. Kramer, T. Polcar, R. Yang, D. Shi, G. Zhang, Ultra-low friction and edge-pinning effect in large-lattice-mismatch van der Waals heterostructures. *Nat. Mater.* **21**, 47–53 (2022).
9. T. Chari, R. Ribeiro-Palau, C. R. Dean, K. Shepard, Resistivity of rotated graphite–graphene contacts. *Nano Lett.* **16**, 4477–4482 (2016).

10. E. Koren, I. Leven, E. Lörtscher, A. Knoll, O. Hod, U. Duerig, Coherent commensurate electronic states at the interface between misoriented graphene layers. *Nat. Nanotechnol.* **11**, 752–757 (2016).
11. R. Ribeiro-Palau, C. Zhang, K. Watanabe, T. Taniguchi, J. Hone, C. R. Dean, Twistable electronics with dynamically rotatable heterostructures. *Science* **361**, 690–693 (2018).
12. N. R. Finney, M. Yankowitz, L. Muraleetharan, K. Watanabe, T. Taniguchi, C. R. Dean, J. Hone, Tunable crystal symmetry in graphene–boron nitride heterostructures with coexisting moiré superlattices. *Nat. Nanotechnol.* **14**, 1029–1034 (2019).
13. D. Dietzel, A. S. de Wijn, M. Vorholzer, A. Schirmeisen, Friction fluctuations of gold nanoparticles in the superlubric regime. *Nanotechnology* **29**, 155702 (2018).
14. D. Dietzel, M. Feldmann, U. D. Schwarz, H. Fuchs, A. Schirmeisen, Scaling laws of structural lubricity. *Phys. Rev. Lett.* **111**, 235502 (2013).
15. L. Banszerus, A. Rothstein, E. Icking, S. Möller, K. Watanabe, T. Taniguchi, C. Stampfer, C. Volk, Tunable interdot coupling in few-electron bilayer graphene double quantum dots. *Appl. Phys. Lett.* **118**, 103101 (2021).
16. L. A. Cohen, N. L. Samuelson, T. Wang, K. Klocke, C. C. Reeves, T. Taniguchi, K. Watanabe, S. Vijay, M. P. Zaletel, A. F. Young, Tunable fractional quantum Hall point contacts in graphene via local anodic oxidation of graphite gates. arXiv:2204.10296 [cond-mat.mes-hall] (21 April 2022).
17. H. Overweg, H. Eggimann, X. Chen, S. Slizovskiy, M. Eich, R. Pisoni, Y. Lee, P. Rickhaus, K. Watanabe, T. Taniguchi, V. Fal'ko, T. Ihn, K. Ensslin, Electrostatically induced quantum point contacts in bilayer graphene. *Nano Lett.* **18**, 553–559 (2018).
18. C. Déprez, L. Veyrat, H. Vignaud, G. Nayak, K. Watanabe, T. Taniguchi, F. Gay, H. Sellier, B. Sacépé, A tunable Fabry–Pérot quantum Hall interferometer in graphene. *Nat. Nanotechnol.* **16**, 555–562 (2021).
19. J. Nakamura, S. Liang, G. C. Gardner, M. J. Manfra, Direct observation of anyonic braiding statistics. *Nat. Phys.* **16**, 931–936 (2020).
20. A. F. Young, C. R. Dean, L. Wang, H. Ren, P. Cadden-Zimansky, K. Watanabe, T. Taniguchi, J. Hone, K. L. Shepard, P. Kim, Spin and valley quantum Hall ferromagnetism in graphene. *Nat. Phys.* **8**, 550–556 (2012).
21. K. Zimmermann, A. Jordan, F. Gay, K. Watanabe, T. Taniguchi, Z. Han, V. Bouchiat, H. Sellier, B. Sacépé, Tunable transmission of quantum Hall edge channels with full degeneracy lifting in split-gated graphene devices. *Nat. Commun.* **8**, 14983 (2017).
22. Y. Ronen, T. Werkmeister, D. Haie Najafabadi, A. T. Pierce, L. E. Anderson, Y. J. Shin, S. Y. Lee, Y. H. Lee, B. Johnson, K. Watanabe, T. Taniguchi, A. Yacoby, P. Kim, Aharonov–Bohm effect in graphene-based Fabry–Pérot quantum Hall interferometers. *Nat. Nanotechnol.* **16**, 563–569 (2021).
23. X. Zhao, M. Hamilton, W. G. Sawyer, S. S. Perry, Thermally activated friction. *Tribol. Lett.* **27**, 113–117 (2007).
24. M. A. Topinka, B. J. LeRoy, S. E. J. Shaw, E. J. Heller, R. M. Westervelt, K. D. Maranowski, A. C. Gossard, Imaging coherent electron flow from a quantum point contact. *Science* **289**, 2323–2326 (2000).
25. J. Xue, J. Sanchez-Yamagishi, D. Bulmash, P. Jacquod, A. Deshpande, K. Watanabe, T. Taniguchi, P. Jarillo-Herrero, B. J. LeRoy, Scanning tunnelling microscopy and spectroscopy of ultra-flat graphene on hexagonal boron nitride. *Nat. Mater.* **10**, 282–285 (2011).
26. M. Fujimoto, H. Koschke, M. Koshino, Topological charge pumping by a sliding moiré pattern. *Phys. Rev. B.* **101**, 041112 (2020).
27. Y. Zhang, Y. Gao, D. Xiao, Topological charge pumping in twisted bilayer graphene. *Phys. Rev. B.* **101**, 041410 (2020).
28. Y. Su, S.-Z. Lin, Topological sliding moiré heterostructure. *Phys. Rev. B* **101**, 041113 (2020).
29. F. Pizzocchero, L. Gammelgaard, B. S. Jessen, J. M. Caridad, L. Wang, J. Hone, P. Bøggild, T. J. Booth, The hot pick-up technique for batch assembly of van der Waals heterostructures. *Nat. Commun.* **7**, 11894 (2016).
30. D. G. Purdie, N. M. Pugno, T. Taniguchi, K. Watanabe, A. C. Ferrari, A. Lombardo, Cleaning interfaces in layered materials heterostructures. *Nat. Commun.* **9**, 5387 (2018).

Acknowledgments: We acknowledge the use of facilities and instrumentation at the Integrated Nanosystems Research Facility (INRF), in the Samueli School of Engineering at the University of California Irvine, and at the UC Irvine Materials Research Institute (IMRI), which is supported in part by the NSF MRSEC through the UC Irvine Center for Complex and Active Materials. We also acknowledge the use of the UCI Laser Spectroscopy Laboratory. We thank L. Jauregui and M. Yankowitz for productive discussions, as well as the technical assistance of Q. Lin, R. Chang, M. Kebali, J. Hes, and D. Fishman. **Funding:** This work was supported by National Science Foundation Career Award DMR-2046849. I.S. acknowledges fellowship support from the UCI Eddleman Quantum Institute. **Author contributions:** Investigation: A.Z.B., I.S., Y.Y., A.H.B.-A., and J.D.S.-Y. Sample preparation: A.Z.B., I.S., and A.H.B.-A. Supervision: J.D.S.-Y. Writing and review: A.Z.B., I.S., J.D.S.-Y., and A.H.B.-A. hBN crystal growth: T.T. and K.W. **Competing interests:** The authors declare that they have no competing interests. **Data and materials availability:** All data needed to evaluate the conclusions in the paper are present in the paper and/or the Supplementary Materials.

Submitted 29 November 2022
Accepted 7 March 2023
Published 7 April 2023
10.1126/sciadv.adf9558

ScienceAdvances

Mechanically reconfigurable van der Waals devices via low-friction gold sliding

Andrew Z. Barabas, Ian Sequeira, Yuhui Yang, Aaron H. Barajas-Aguilar, Takashi Taniguchi, Kenji Watanabe, and Javier D. Sanchez-Yamagishi

Sci. Adv., **9** (14), eadf9558.
DOI: 10.1126/sciadv.adf9558

Science Advances (ISSN) is published by the American Association for the Advancement of Science. 1200 New York Avenue NW, Washington, DC 20005. The title *Science Advances* is a registered trademark of AAAS.